

Extreme Scattering Events Towards Two Young Pulsars

M. Kerr^{1*}, W. A. Coles², C. A. Ward^{3,4}, S. Johnston³, A. V. Tuntsov⁵,
and R. M. Shannon³

¹*Space Science Division, Naval Research Laboratory, Washington, DC 20375-5352, USA*

²*ECE Department, University of California at San Diego, La Jolla, CA 92093-0407, USA*

³*CSIRO Astronomy and Space Science, Australia Telescope National Facility, PO Box 76, Epping NSW 1710, Australia*

⁴*Sydney Institute for Astronomy, School of Physics, University of Sydney, NSW 2006, Australia*

⁵*Manly Astrophysics, 15/41-42 East Esplanade, Manly, NSW 2095, Australia*

Accepted 2017 November 22. Received 2017 November 22; in original form 2017 September 15

ABSTRACT

We have measured the scintillation properties of 151 young, energetic pulsars with the Parkes radio telescope and have identified two extreme scattering events (ESEs). Towards PSR J1057–5226 we discovered a three-year span of strengthened scattering during which the variability in flux density and the scintillation bandwidth decreased markedly. The transverse size of the scattering region is ~ 23 au, and strong flux density enhancement before and after the ESE may arise from refractive focusing. Long observations reveal scintillation arcs characteristic of interference between rays scattered at large angles, and the clearest arcs appear during the ESE. The arcs suggest scattering by a screen 100–200 pc from the earth, perhaps ionized filamentary structure associated with the boundary of the local bubble(s).

Towards PSR J1740–3015 we observed a “double dip” in the measured flux density similar to ESEs observed towards compact extragalactic radio sources. The observed shape is consistent with that produced by a many-au scale diverging plasma lens with electron density ~ 500 cm⁻³. The continuing ESE is at least 1500 d long, making it the longest detected event to date.

These detections, with materially different observational signatures, indicate that well-calibrated pulsar monitoring is a keen tool for ESE detection and ISM diagnostics. They illustrate the strong rôle au-scale non-Kolmogorov density fluctuations and the local ISM structure play in such events and are key to understanding both their intrinsic physics and their impact on other phenomena, particularly fast radio bursts.

Key words: pulsars:general, ISM:structure

1 INTRODUCTION

The discovery of dramatic variations in the observed flux density of the quasar 0954+658 (Fiedler et al. 1987), dubbed an “extreme scattering event”, revealed an unexpected and poorly understood property of the ionized interstellar medium (ISM). If produced by refraction (Romani et al. 1987), the required column density gradients imply densities ≥ 1000 cm⁻³ for symmetric distributions and are consequently overpressured relative to the ambient ISM by three orders of magnitude. Various mechanisms, from local density enhancements (Walker & Wardle 1998) to highly asymmetric structures like current sheets (Pen & King 2012) and circumstellar plasma streams (Walker et al. 2017) have been

proposed to alleviate this overpressure problem, but the origin of the structure remains unclear.

A primary difficulty in advancing the field is the relative rarity of such events. They are typically discovered in archival data and thus lack the contemporaneous VLBI/multi-frequency observations that help probe the lensing structure. Only recently was an ESE detected and studied in real time via a monitoring campaign of bright extragalactic AGN (Bannister et al. 2016), and the wide frequency coverage and VLBI imaging provided detailed insight into the electron column density profile (Tuntsov et al. 2016).

While dedicated campaigns like those of Bannister et al. (2016) will continue to turn up new ESEs, we point out pulsar monitoring as a complementary approach. Indeed, pulsar point sources are ideal for detecting ESEs since the ESE signature is not convolved with a finite source geometry. Fur-

* E-mail: matthew.kerr@gmail.com

Table 1. Fiducial scattering model values for PSR J1057–5226 for observing frequency 1369 MHz and screen at $\zeta = 1/2$.

Distance (D , pc)	400
Dispersion Measure (DM, e^{-1} pc cm^{-3})	30.1
Transverse velocity (km/s)	80
Fresnel radius (cm)	6.5×10^{10}
Decorrelation bandwidth (B_d , MHz) ...	50
Decorrelation time-scale (s)	1000
Diffractive scale (s_d , cm)	4.4×10^9
Refractive scale (cm)	9.6×10^{11}
Diffractive time-scale (s)	1100
Refractive time-scale (hr)	66

ther, examination of differential delays in pulse arrival times admits direct measurement of the electron column density (dispersion measure, DM) towards the source. Coles et al. (2015) identified two ESEs towards millisecond pulsars via their variations in DM and scintillation strength, and there are likely a spectrum of less extreme events in the dataset, making ISM studies a fruitful offshoot of the effort to detect low-frequency gravitational waves by pulsar timing arrays. However, MSPs are much rarer than unrecycled pulsars and so probe few lines of sight. Thus, with an aim towards discovering new ESEs, we searched over 1200 source-years of data taken for the young pulsar timing program on the Parkes telescope (Weltevrede et al. 2010, “P574”).

We discovered two clear ESEs with dramatically different observational signatures. One, towards PSR J1740–3015, is a smooth modulation of the pulsar light curve reminiscent of the Fiedler et al. event and suggestive of coherent lensing by a plasma structure. The other, towards PSR J1057–5226, is more like the events reported by Coles et al. (2015), detected through modification of diffractive scintillation properties. Although this latter type, observed exclusively towards pulsars, have not been identified as ESEs in the literature until recently, they too are caused by au-scale inhomogeneities that cross the line of sight and substantially alter/dominate the scattering properties. It is only in the addition of diffractive effects from the pointlike sources that their observational signature differs, and accordingly we classify both episodes as ESEs.

In §2, we discuss the P574 observations and the production of the dynamic spectra on which this analysis is based. We follow in §3 with a discussion of PSR J1057–5226, its scintillating nature, and the ESE detected towards it. We do the same for PSR J1740–3015 in §4. In §5, we offer interpretation of the observations.

2 OBSERVATIONS AND DATA REDUCTION

We observed PSRs J1057–5226 and J1740–3015 as part of a continuing program to time about 150 young (characteristic ages $10^{5 \pm 0.5}$ yr), energetic ($\dot{E} > 10^{34}$ erg s^{-1}) pulsars with the Parkes radio telescope to provide rotational ephemerides for γ -ray analysis with the *Fermi* Large Area Telescope. The program has been extremely successful both in its original purpose (Abdo et al. 2013, nearly 40 γ -ray pulsars discovered using Parkes data) and through the study of the wealth of pulse profiles and timing data (e.g. Rookyard et al. 2017; Brook et al. 2016; Antonopoulou et al. 2015; Karastergiou

et al. 2011). The data set, now spanning more than eight years, allows detection of phenomena with time-scales of several years, e.g. DM variations (Petroff et al. 2013) and the recently discovered quasi-periodic modulations in the pulse times of arrival of eight members of the sample (Kerr et al. 2016). Many of the pulsars in the sample have large DMs and are (very) strongly scattered by the ISM. As pulsars become more strongly scattered, their diffractive time-scale (the period over which the observed intensity in a narrow band becomes decorrelated) becomes shorter while their refractive time-scale (over which the line-of-sight crosses the scattering disk) becomes longer, due to the increased size of the scattering disk, reaching months to years for typical lines of sight in the Galactic plane. These time-scales can be measured by studying the correlations in pulsar light curves (e.g. Kaspi & Stinebring 1992), prompting us to produce flux-density calibrated light curves from our timing observations as follows.

The pulsar sample was observed with a roughly monthly cadence with short, two or three-minute snapshot observations using primarily the centre pixel of the 20 cm multi-beam receiver. For about six months in 2007 and in 2016, we used another 20 cm (“H-OH”) receiver. We recorded 256 MHz of bandwidth centred on 1369 MHz using a succession of digital polyphase filterbanks systems (PDFB1-PDFB4) and folded the resulting 1024 spectral channels into pulse profiles with 1024 phase bins. (With the H-OH receiver in 2016, we recorded 2048 channels over 512 MHz of bandwidth at 1465 MHz.) To measure the differential gains between the signal paths of the two voltage probes, once an hour we observe a pulsed noise signal injected into the signal path prior to the first-stage low-noise amplifiers. The noise signal also provides a reference brightness for each observation. To correct for the absolute gain of the system, we make use of observations of the radio galaxy 3C 218 (Hydra A); by using on- and off-source pointings, we can measure the apparent brightness of the noise diode as a function of radio frequency. Finally, to measure the flux density, we cross-correlate the observed profile with a standard template. For the total flux density at each epoch, we have integrated over the observing band and observation duration, while for the dynamic spectra we retain the native resolution of the filterbanks. All data reduction makes use of the PSRCHIVE (Hotan et al. 2004) software package.

Dynamic spectra are particularly sensitive to radio-frequency interference (RFI) as both quasi-stationary narrowband and impulsive broadband signals can create spurious enhancements of frequency and time intervals. To mitigate RFI and aliasing, we filter out the edges of the band (5%) and channels exceeding a median-smoothed bandpass, and we identify sub-integrations affected by impulsive RFI by eye and remove them. These missing channels and sub-integrations introduce additional windowing to the secondary spectra discussed below, but the percentage of filtered data is typically small. When constructing secondary spectra, we linearly interpolate over missing data to minimize windowing artifacts. Large features in dynamic spectra such as bright scintles manifest as low-frequency power in secondary spectra and, due to windowing from finite observation length, can leak to higher power. We partially mitigate this in affected observations by first-order differencing (pre-whitening) and subsequent correction of the output

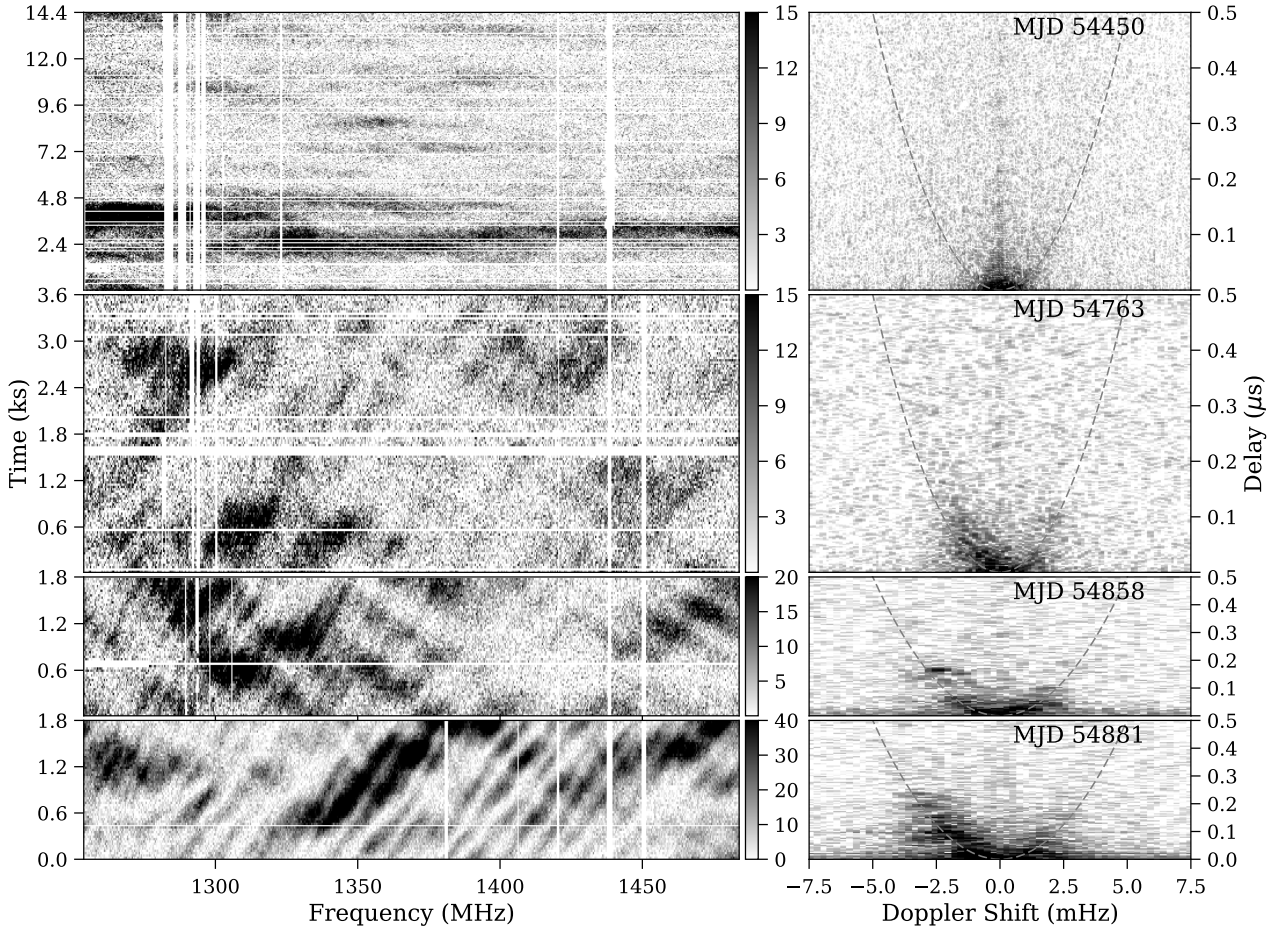


Figure 1. Dynamic and secondary spectra for observations of PSR J1057–5226 in 2007 and 2008. Left: Greyscale gives flux density in mJy. Dynamic spectra generally have different durations and pixel scales. Right: The secondary spectra are not to scale, but all share the same axes bounds. The greyscale floor is set at the white noise level, and the maximum three decades above. The model arcs are drawn with $a = 0.02\text{ s}^3$, the predicted value for our fiducial distance/velocity model (eqs. 1 and 2)

spectrum (post-darkening); see Coles et al. (2011) for more details.

3 PSR J1057–5226

PSR J1057–5226 (B1055–52) is a bright pulsar discovered in the seminal, early pulsar search survey of the southern sky by Vaughan & Large (1972). Its high S/N profile has furnished several insights into the pulsar mechanism (Weltevrede et al. 2012) and it is one of the brightest γ -ray pulsars in the sky. Indeed, the constraints from its radio polarimetry and γ -ray light curve together provide some of the first evidence for “backwards” γ -ray beams (Craig 2015). PSR J1057–5226 has also been detected at optical and UV wavelengths using the *Hubble* Space Telescope, allowing sensitive astrometry and refined spectral distance estimates as we review below.

3.1 Distance and Velocity

The interpretation of scintillation measurements depends critically on the distance and velocity of a pulsar, but unfortunately the distance to PSR J1057–5226 is not well

constrained. According to the electron distribution model of Taylor & Cordes (1993), the modest DM (30.1 pc cm^{-3}) places it at a distance of 1.53 kpc, but more modern models place it at 0.72 kpc (NE2001 Cordes & Lazio 2002) and 94 pc (YMW16 Yao et al. 2017), an order of magnitude discrepancy. Constraints from other observations place the pulsar in the lower half of this range. Mignani et al. (2010), by modelling of the optical, UV, and X-ray spectrum, estimate a distance of 400 pc. The high γ -ray efficiency, 25.6% at 400 pc (Abdo et al. 2013), also suggests a true distance at the lower end of this range, and we therefore adopt a fiducial distance of 400 pc.

Mignani et al. (2010) measure a proper motion of $42 \pm 5\text{ mas yr}^{-1}$ by comparing the *Hubble* position with an archival radio timing position. At our fiducial distance, this leads to a transverse velocity of 80 km s^{-1} , somewhat low but consistent with typical two-dimensional speeds (median $\sim 180\text{ km s}^{-1}$, Hobbs et al. 2005). However, due to timing noise and the relatively short span of data used in producing the archival radio position, we sought to verify the proper motion using a single long span of pulsar timing data.

Archival data from Parkes observations are available with varying cadence from 1992 and include a range of instruments and receivers. The raw data are currently unavail-

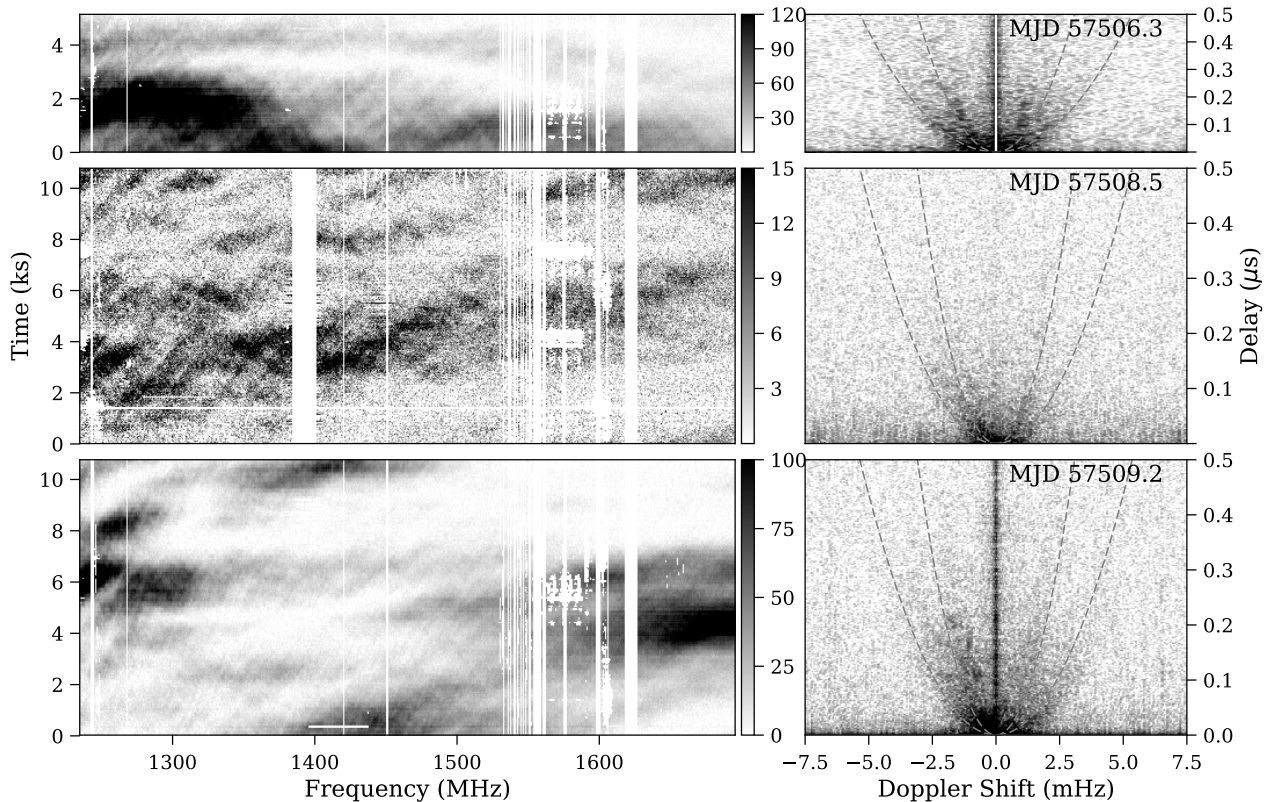


Figure 2. Left: A sequence of dynamic spectra of PSR J1057–5226 taken with the H-OH receiver on three consecutive days. Right: The corresponding secondary spectra. Note that the power along the axes of 0 mHz and 0 μ s is largely due to spectral leakage (see §2), and we have pre-whitened/post-darkened the spectra for MJDs 57506.3 and 57509.2. The parabolae are drawn with $a = 0.02$ (outer) and $a = 0.06 \text{ s}^3$ (inner).

able, so we used a partially-reduced version of the data that were folded at the correct pulsar period and reduced to, typically, 4 or 8 spectral channels. Ultimately, we assembled 2306 pulse times of arrival (TOAs) spanning from July 1992 to January 2016. The noise properties of the TOAs vary strongly over the data span. Radiometer noise generally decreases over time as more sensitive, wider bandwidth systems became available. Early data sometimes suffer pulse profile distortions due to single-bit digitization, and nearly all lack polarization calibration. To account for this noise, we flagged each unique combination of receiver and backend system and modified the TOA errors with an overall scale and an additional error added in quadrature (“EFAC” and “EQUAD”). We also allow each system to have a free phase adjustment (“JUMP”) relative to the fiducial system (PDFB4). Finally, we fit the timing model and these white noise parameters, together with a power law representation of red timing noise, using TEMPO₂ (Lentati et al. 2014). At an epoch of MJD 54531, we find a position

$$\alpha = 10^{\text{h}}57^{\text{m}}58^{\text{s}}.959(4), \delta = -52^{\circ}26'56''.42(4)$$

and a proper motion

$$\mu_{\alpha} \cos \delta = 44 \pm 5 \text{ mas yr}^{-1}, \mu_{\delta} = -6 \pm 5 \text{ mas yr}^{-1},$$

with a total proper motion of $44 \pm 5 \text{ mas yr}^{-1}$, verifying the result of Mignani et al. (2010). Unfortunately, the precision of the parallax measurement is only 60 mas, so we can only place a lower limit on the distance of about 10 pc.

3.2 Scintillation Properties

Refraction contributes most strongly at the transition from weak to strong scattering (e.g. Coles et al. 1987), which occurs when the transverse coherence scale in the scattering medium becomes smaller than the Fresnel radius, or equivalently when the decorrelation bandwidth becomes smaller than the observing frequency ν_0 . Though depending on frequency and the wavenumber spectrum, refraction contributes of order 0.1 (Rickett 1990) to the modulation index ($m \equiv \sigma_F/F$, with F the observed flux density) while diffractive scintillation has $m = 1$. As we show below, we observed $m = 1.2$ for J1057–5226 outside of the ESE, indicating a strong $m = 0.7$ for the refractive component. Thus, even though the observed decorrelation bandwidth for our 20 cm observations is $< \nu_0/20$, formally placing it well into strong scattering, refraction plays an outsize rôle, perhaps indicating the presence of an inner scale in the turbulence spectrum (Coles et al. 1987). Such strong variations may also reflect the presence of discrete refracting structures. The observational consequence of this large variance is that we occasionally see flux densities almost 20 times greater (or lower) than the mean even though our bandwidth encompasses multiple diffractive scintles.

Identifying the “baseline” diffractive properties of PSR J1057–5226 is challenging. Johnston et al. (1998) report values of 36.7 MHz (correlation half-width at half-maximum) and 308 s (correlation half-width at $1/e$) at

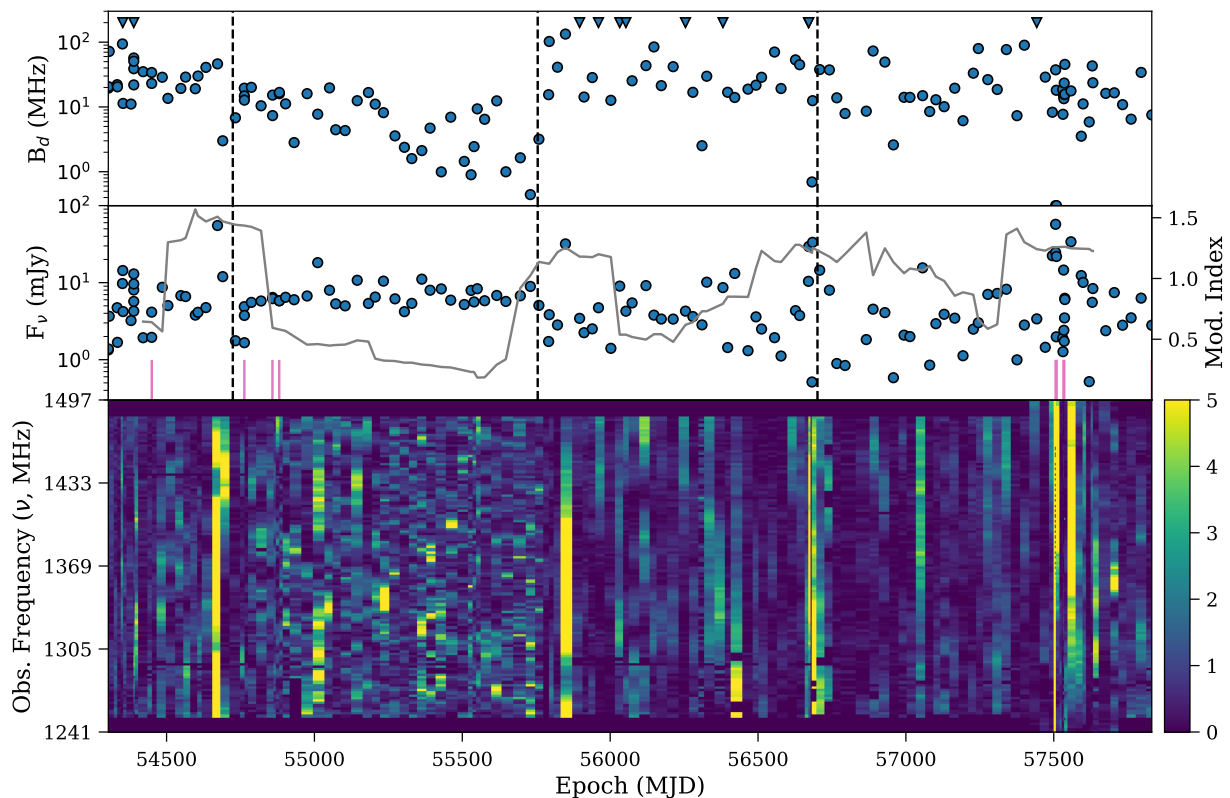


Figure 3. The dynamic spectra, integrated flux density, and measured scintillation bandwidth for PSR J1057–5226 over the full observing span. Top panel: Scintillation bandwidth measurements, obtained by fitting an exponential model to the secondary spectra (see §3.3). Middle panel: Band-averaged flux densities at each epoch and the corresponding modulation index. Both here in the bottom panel, in order to put all observations on the same footing, we have averaged in time over the full observation or over the first three minutes, whichever is shorter. The horizontal red lines show the epochs of the long observations whose secondary spectra we show in Figures 1, 2, 4, and 5. The gray trace shows the modulation index obtained from observations taken within six months of the indicated epoch, and consequently no measurements appear for epochs within six months of the ends of the observing span. Bottom panel: the pulsar spectra from our snapshot observations. The spectra have been normalized to the best-fit mean power law model $F_\nu = 7.04 (\nu/1.4 \text{ GHz})^{-1.09}$ mJy. To better display the large dynamic range, the scale saturates at 5, but outliers range up to about 20.

1388 MHz. However, long observations almost always reveal fringing in the dynamic spectra characteristic of interference between rays scattered from large angles (see below), and these fringes obscure the underlying large-scale scintles from the scattering core. We have identified a few long observations that appear relatively free from such interference (e.g. the top panel of Figure 1) and estimate a slightly larger decorrelation bandwidth of 50 MHz and decorrelation time-scale of 1000 s, which we adopt for a fiducial model.

We can check the consistency of this model by noting that, if the pulsar velocity is dominant, the decorrelation time-scale is simply the time it takes a coherent patch on the scattering screen to translate past the line-of-sight. If the phase variations are due to a Kolmogorov spectrum of fluctuations, then the coherence length $s_d^2 = \zeta(1-\zeta)/2(B_d/\nu_0)r_f^2$, with ζ the normalized distance from the pulsar to the screen, $r_f = \sqrt{\lambda D/2\pi}$ the Fresnel distance, and B_d the diffractive bandwidth. We report these parameters in Table 1 and, if we place the screen halfway to the pulsar, we find the coherence length to be 4.4×10^9 cm. If the effective velocity along the screen is dominated by the pulsar velocity, i.e. is 40 km s^{-1} , then the predicted decorrelation time is 1100 s, in good agreement with our model. The corresponding re-

fraction timescale is 66 hours, somewhat longer but in qualitative agreement with the day-to-day variations we observe (e.g. Figure 2).

3.3 Extreme Scattering Event

We have examined the flux density and diffractive properties of J1057–5226 over our data set and show our results in Figure 3. To measure the decorrelation bandwidth (B_d), we computed the secondary spectrum for each observation (the Fourier transform of the dynamic spectrum) and then fitted the models used by Coles et al. (2015). We have also measured the flux density for each observation. The typical observation length (120 to 180 s) is much shorter than the decorrelation time-scale (1000 s), so they give snapshots whose variance is dominated by the diffractive scintillation structure. This is borne out by the running modulation index, shown in the middle panel of the figure, which reaches values up to ~ 1.2 . In order to put the longer observations on the same footing, we simply truncate those observations to 180 s when measuring the flux density.

There is a substantial drop in both the decorrelation bandwidth and the variance in the snapshot flux density

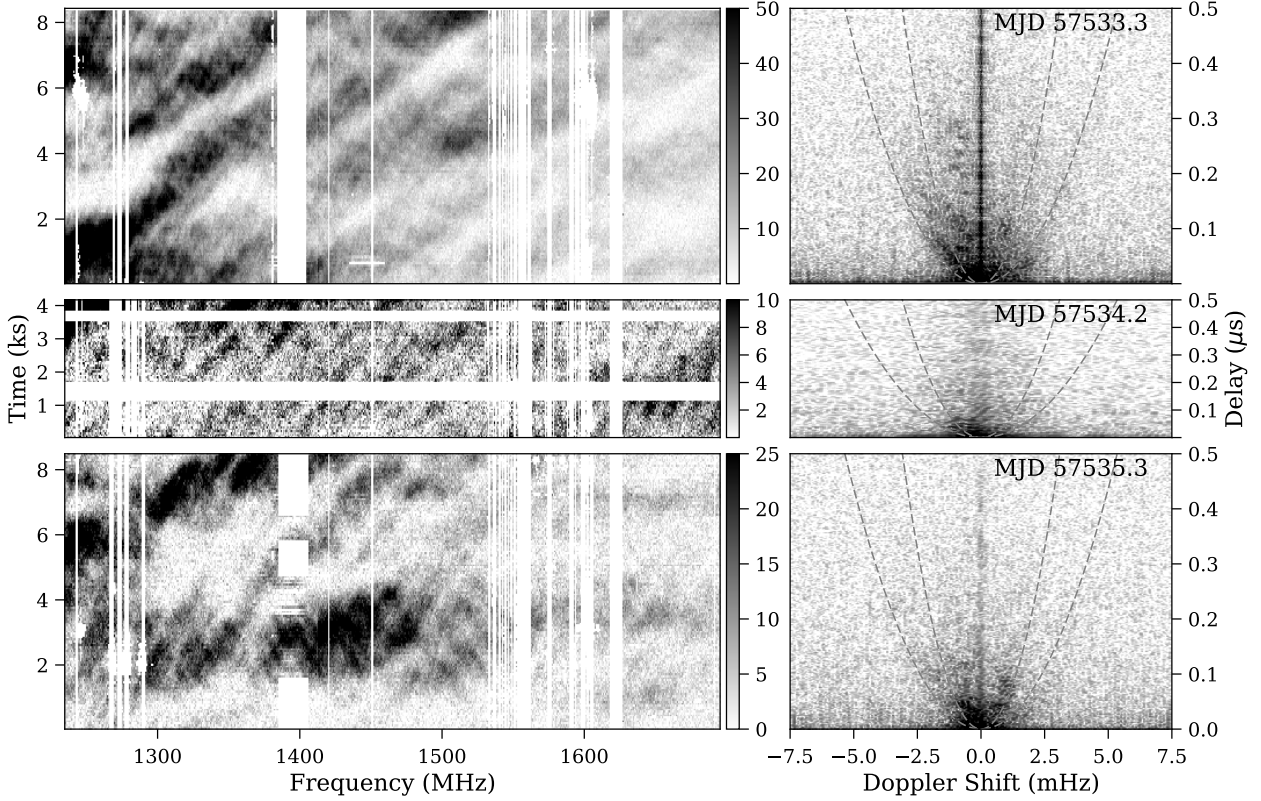


Figure 4. A sequence of PSR J1057–5226 dynamic and secondary spectra taken with the H-OH receiver on three consecutive days. We pre-whitened/post-darkened the secondary spectrum from MJD 57533.3. Parabolae are drawn with $a = 0.02$ (outer) and $a = 0.06 \text{ s}^3$ (inner).

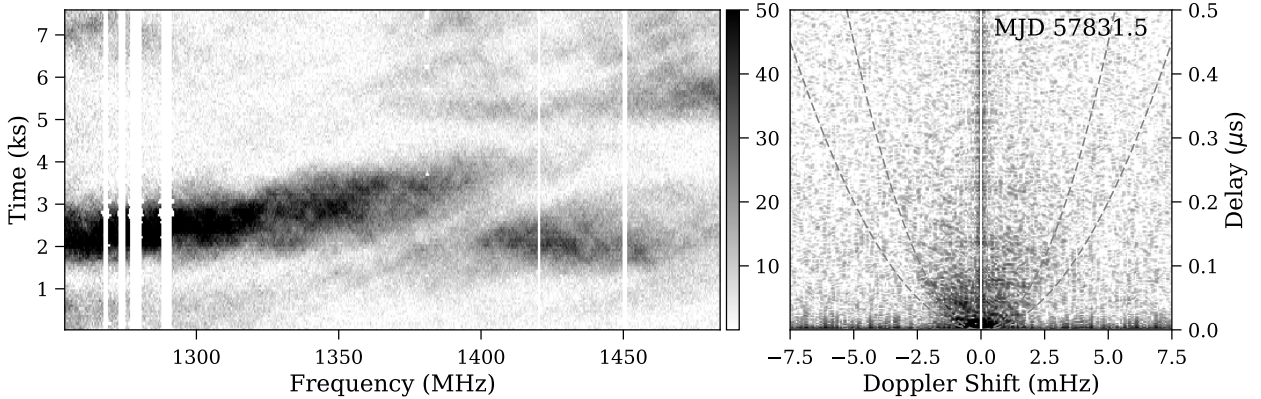


Figure 5. PSR J1057–5226 dynamic and secondary spectrum (with pre-whitening/post-darkening) made in March, 2017 with the multi-beam receiver. Parabolae are drawn with $a = 0.02$ (outer) and $a = 0.06 \text{ s}^3$ (inner).

beginning around MJD 54725 and concluding around MJD 55755, shown as the first two vertical dashed lines in Figure 3. Both are hallmarks of an increase in the scattering strength, and thus the ESE is due to *additional* turbulent plasma entering the line-of-sight. (The flux variance decreases as there are more scintles in the band for stronger scattering, so the snapshot observations approach the mean flux.) There are strong, wideband flux density enhancements preceding and following the ESE. These may be coincidental, or they may be refractive enhancements (lensed emission) associated with the boundary of the scattering structure.

The scattering structure itself cannot lens strongly, as there is no measurable decrease in the mean observed flux.

There is a clear gradient in the diffractive bandwidth over the duration of the ESE, with the scattering strongest in the trailing edge. The sharp delineation in diffractive bandwidth makes the event duration a relatively precise $1000 \pm 50 \text{ d}$. However, its linear size depends on where it lies along the line of sight. If we take it as halfway to pulsar ($\zeta = 1/2$), and again assign the dominant motion to the pulsar velocity ($V_{\text{eff}} = 40 \text{ km s}^{-1}$), the transverse size is $23 (V_{\text{eff}}/40 \text{ km s}^{-1}) \text{ au}$. This is substantially larger than

structures reported for other ESEs, even if it is much closer with a typical local relative velocity of 10 km s^{-1} .

We have marked an additional event at MJD 56700, a series of very bright observations bookending a near non-detection. These may also represent a small plasma lens crossing the line of sight, with characteristic caustic enhancements preceding and following a defocused region (e.g. Clegg et al. 1998). The decorrelation bandwidth appears to decrease slightly following this event.

There are additional less “extreme” but similar events. Around MJD 56300 the drop in modulation index is accompanied by a single observation with a markedly decreased scintillation bandwidth, reminiscent of (but in the opposite sense to) the “pinhole” in DM reported by Coles et al. (2015) for PSR J1713+0747.

3.4 Large-angle Scattering

Although fringing in pulsar dynamic spectra had been appreciated for some time as a realization of multiple imaging (Rickett 1990), it was the discovery of dramatic parabolic arcs in secondary spectra (Stinebring et al. 2001) that crystallized the understanding that these features are the natural hallmarks of a medium capable of supporting wide-angle scattering (Walker et al. 2004; Cordes et al. 2006) and that they are a sensitive probe of the angular scattering spectrum. Briefly, in the case of interference between a dominant small-angle scattering core and a halo of light scattered at larger angles, the scattered waves will be Doppler shifted (f_t) by the screen velocity an amount proportional to the scattering angle and will suffer a delay (f_ν) proportional to its square. The scattering halo sites then map onto a parabola

$$f_\nu = a f_t^2 \quad (1)$$

(see equation 11 of Cordes et al. (2006), NB in the second equality the signs of the exponents of the velocity and units are inverted), with

$$a = 0.116 \times 4 \zeta(1 - \zeta) D \nu^{-2} V_{\text{eff}}^{-2} s^3, \quad (2)$$

with D the pulsar distance in kpc, ν the observing frequency in GHz, and V_{eff} the projected screen velocity scaled by 100 km s^{-1} . Therefore, in addition to the snapshot spectra discussed above, we have analyzed long archival observations, taken primarily in 2007 and 2008, as well as recent data obtained after the discovery of the ESE. These long observations provide the necessary resolution to identify scattering features in secondary spectra.

A very long observation in 2007 (Figure 1, top panel) gives a reasonable representation of the “baseline” scattering state of PSR J1057–5226. Large structures in frequency and time, with a strong refractive enhancement in the first part of the observation, yield a dense knot of scattering near the origin in the secondary spectrum; the dimensions of this knot yield the canonical diffractive scintillation bandwidth and time-scale. The next long archival observations occur in 2008, after the onset of the ESE. The first such observation, the second from the top, shows obvious fringing, and the secondary spectrum reveals these fringes as power well removed from the origin, with negative Doppler shifts of a few mHz and delays of up to $0.1 \mu\text{s}$, while the subsequent two observations show features with delays up to $0.25 \mu\text{s}$. For our fiducial model with $D = 0.4$, $\zeta = 1/2$, and $V_{\text{eff}} = 40 \text{ km s}^{-1}$,

$a = 0.02 \text{ s}^3$, shown as dashed arc drawn in Figure 1 and in good agreement with the observed curvature. This agreement reinforces our fiducial distance and velocity model and again suggests the ESE is $>20 \text{ au}$. in transverse dimension.

We have observed similar, if less pronounced, fringing in recent observations taken as a dedicated followup to the discovery of the ESE. In a series of observations made on subsequent days in late April/early May 2016 (Figure 2), there is evidence both of strong refractive enhancement and of scattering structure apparently associated with an even greater value of $a = 0.06 \text{ s}^3$. The scintillation arc evolves rapidly on a 1-day time-scale, with the power along the arc at positive Doppler shift on the first day fading over the two subsequent days. The time required for this material to translate far enough to escape the scattering region is about 50 d, so this variability must reflect the scattering process itself. Indeed, Coles et al. (2010) found such variation in arc asymmetry on refractive time-scales in simulations of Kolmogorov turbulence.

Another series of consecutive long observations at the end of May 2016 shows a similar evolution (Figure 4). The first observation reveals scattering at large delay ($0.3 \mu\text{s}$) and small negative Doppler shift (-1 mHz), and there is extremely strong low-frequency fringing. Two days later, that structure has largely vanished, while substantial power at small scattering angles, along the inner parabola, has appeared. A final long observation made in March of 2017 (Figure 5) reveals a symmetric distribution concentrated at the origin, suggesting absence of large-angle interference.

If the larger value of a is a distinct feature, and if the effective velocity remains dominated by the pulsar velocity, then the screen distances are related by $a_1/a_2 = \zeta_1(1 - \zeta_2)/\zeta_2(1 - \zeta_1)$. If $\zeta_1 = 1/2$ during the ESE is correct, then $\zeta_2 = 3/4$. That is, the “baseline” screen is located $1/4$ of the way from the earth to the pulsar, and halfway between the ESE screen and the earth. Since there is also still power filling the area between the two parabolae (particularly during the strong fringing on MJD 57533), this suggests scattering occurs over an extended region from $100\text{--}200 \text{ pc}$.

Finally, under the assumption that the scattering is dominated by bright core/large angle interference, the secondary spectrum can be directly mapped to a brightness distribution. For our fiducial model, a parabola following $a = 0.02 \text{ s}^3$ yields an approximately circular brightness distribution, while smaller (larger) values are elongated along the (perpendicular to the) effective velocity vector. Thus, the brightness distribution is circular during the ESE (save for the bright large angle knot) but somewhat elongated perpendicular to the velocity in subsequent epochs. In fact, change of image shape may also be sufficient to explain the different apparent values of a , as asymmetry in the image strongly affects the position of scattered power relative to the predicted parabola (e.g. Cordes et al. 2006).

4 PSR J1740–3015

PSR J1740–3015 (B1737–30), discovered by Clifton & Lyne (1986) at a DM of 152 pc cm^{-3} , is a radio-bright but otherwise unremarkable pulsar, save for its relatively frequent glitches (Clifton & Lyne 1986). Its precise distance remains unknown. Johnston et al. (2001) were able to detect HI ab-

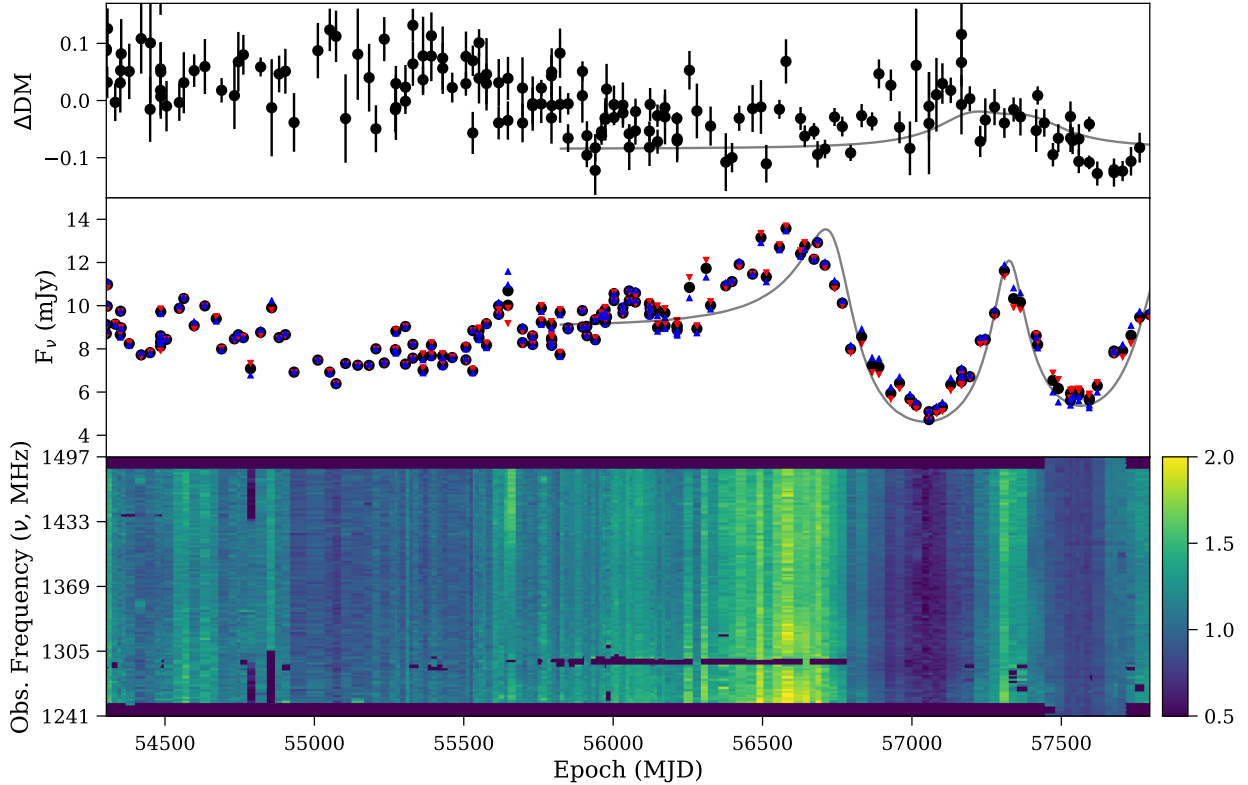


Figure 6. The DM variation, light curve, and dynamic spectra for PSR J1740–3015 over the full observing span. Top: The DM as estimated from in-band pulsar timing. The gray trace shows the predicted DM from the simple lens model described in §4.2. Middle: The band-averaged flux density (black circles) and the flux density for the top (blue upward-pointing triangles) and bottom (red downward-pointing triangles) halves of the band after scaling for the mean spectral index. The gray trace shows the flux variations predicted by the simple lens model. Bottom: the dynamic spectrum, averaged over time, for each observing epoch. The spectra have been normalized to the best-fit mean power law model $F_\nu = 7.58 (\nu/1.4 \text{ GHz})^{-1.05} \text{ mJy}$.

Table 2. Fiducial scattering model values for PSR J1740–3015 for observing frequency 1369 MHz and screen at $\zeta = 1/2$.

Distance (D , kpc)	2.0
Dispersion Measure (DM, $e^{-1} \text{ pc cm}^{-3}$)	152
Transverse velocity (km s^{-1})	150
Fresnel radius (cm)	1.5×10^{11}
Decorrelation bandwidth (B_d , MHz) ...	1
Decorrelation time-scale (s)	–
Diffractive scale (s_d cm)	1.4×10^9
Refractive scale (cm)	1.6×10^{13}
Diffractive time-scale (s)	190
Refractive time-scale (d)	24

sorption at 15 km s^{-1} , but the 3 kpc arm is seen only in emission, leading those authors to conclude only that the pulsar is nearer than $5.5 \pm 0.6 \text{ kpc}$. Verbiest et al. (2012) more recently invoked Malmquist bias to suggest that the distance is only $0.4^{+1.7}_{-0.3} \text{ kpc}$. Both the NE2001 and the YMW16 DM/distance models predict intermediate distances of 2.7 and 2.9 kpc, respectively. Due to the lack of any obvious strongly-ionized regions along the line-of-sight and the small decorrelation bandwidth (see below), we favour these intermediate distances and adopt a fiducial pulsar distance of 2.0 kpc, marginally consistent with the large uncertainties of Verbiest et al. (2012). Unfortunately, there are no con-

straints on the pulsar proper motion, and we adopt a typical speed of 150 km s^{-1} .

We note that PSR J1740–3015 lies at an ecliptic latitude of -6.9° , and consequently in December passes very close to the sun, with some observations having a solar angle $< 10^\circ$. Such observations (about ten in our set) suffer a degraded system temperature and additional bandpass ripple from standing waves between the telescope focus and antenna surface. However, we find no evidence that the post-calibration spectra are out of trend and we do not exclude these data.

4.1 Scintillation Properties

Measurements of the correlation bandwidth, as well as inspection of Figure 6, indicate the scintillation bandwidth is $\sim 1 \text{ MHz}$, making the measurement via correlation of channels of marginal reliability. We also evaluated the scintillation bandwidth by measuring excess variance in the dynamic spectra. In brief, the total variance within a sub-integration should be equal to the radiometer contribution plus a χ^2_{2n} , with n the number of scintles within the band. Because intrinsic variation in pulse amplitude and shape (“jitter”) is typically correlated over bandwidths much larger than the observing bandwidth (Shannon et al. 2014), its noise contribution is negligible. The typical excess variance, corre-

sponding to a value of $n = 220$ in a 256 MHz band, confirms a ~ 1 MHz bandwidth. The baseline model values with our fiducial distance and velocity are given in Table 2.

After removing the low-frequency trend from the measured flux densities (middle panel of Figure 6), the band-integrated modulation index is about 0.07. The expected variance from DISS is 5–10%, indicating residual contributions from refraction at a 24-day time-scale are minimal. However, there is clearly variation on longer time-scales. Due to the low ecliptic latitude, the orbital motion of the earth may be substantial relative to the scattering medium, leading to an annual signal. However, when we computed a power spectrum of the long-term light curve (by interpolating and pre-whitening/post-darkening to correct for spectral leakage) we found no clear quasi-periodic signal.

4.2 Extreme Scattering Event

Above the level of refractive variation, there is a clear increase in received flux density beginning at MJD 56250, though the leading edge may extend earlier in time. Relative to a baseline flux density of 8 mJy, the ESE peaks around 13 mJy (163%), followed by a dip to 5 mJy (61%). A second more moderate (11.5 mJy) peak and trough (5.8 mJy) follow. In a typical diverging lens geometry, at least one more peak is expected. During the ESE, there appears to be a low-frequency ripple in the intensity across the observing band (bottom panel), with greater intensity towards the edges and a clear dip in the band center; this variation is most clearly visible near the first intensity peak at MJD 56600. We have also plotted the flux density for the top and bottom halves of the observing band, scaled to the mean spectral index, as triangles in the middle panel. These light curves show that the ESE is frequency-independent over our observing band.

This is the longest ESE observed to date. Maitia et al. (2003) report a three-year ESE towards the millisecond pulsar J1643–1224, but this is likely a special case of a persistent annual modulation related to the earth’s orbital motion (Keith et al. 2013). The duration of this ESE is already at least 1550 d, and if the expected second peak is similar in shape to the first, the total length will be around 2000 d.

Following Clegg et al. (1998), we have modelled the flux density modulation as a diverging plasma lens crossing the line-of-sight. The two dips require two modes in the distribution, and we compute the received flux density using simple ray tracing, taking into account the finite source distance. The resulting model, at our fiducial screen distance of 1000 pc, appears in Figure 7. In this model, the two Lorentzian components with HWHM w have separation $0.68w$ and the trailing component column density N_e amplitude is 80% of the first. We note that Gaussian components provide a poorer fit as modulation between the peaks is too deep. With the effective screen velocity of 75 km s^{-1} , the predicted transverse size of $\sim 80 \text{ au}$ is in good qualitative agreement with the data. The finite distance of the source means the inferred lens size is smaller than one in the plane wave approximation.

This model is not unique. Even setting aside more complicated (e.g. 2-d) lens shapes, there is degeneracy between the lens distance, electron column density (N_e), and size (Clegg et al. 1998), and here a two-parameter family of lenses provides a good description of the data. The assumed trans-

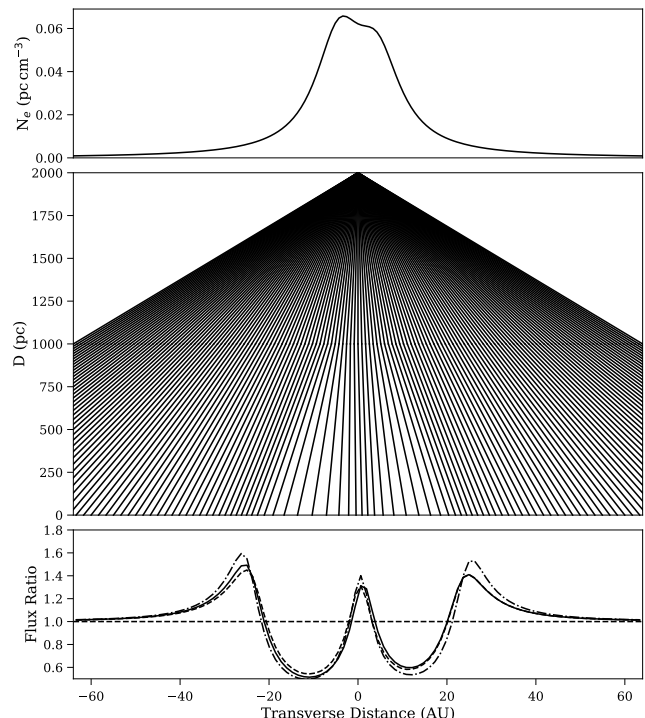


Figure 7. A diverging plasma lens model for the J1740–3015 ESE. Top: the predicted electron column density in typical DM units. Middle: The evolution of the field in the geometric approximation. Bottom: The received intensity.

verse velocity fixes the lens size at a given distance to be $w = 6.4 \text{ au} (D_l/1 \text{ kpc})(V_0/75 \text{ km s}^{-1})$, and the peak/trough amplitude then requires the normalization column density to follow $N_e = 0.050 \text{ pc cm}^{-3} (D/1 \text{ kpc})(V_0/75 \text{ km s}^{-1})^2$. Here, V_0 represents the normalization of the transverse screen velocity, scaled in such a way that the observed ESE length is correct at the other model values. This scaling has two important consequences.

First, we obtain equally good results over a broad range of lens distances. However, small lens distances can be ruled out because the image scale becomes too small to account for the long ESE with reasonable relative velocities. More distant lenses require greater electron column depths, and for lenses further than about 1 kpc the required column would exceed our observational constraints on DM variation. In the top panel of Figure 6, we show the DM as computed by fitting with TEMPO2 a ν^{-2} dispersion model to 8 TOAs extracted across the observing band along with the DM column for our fiducial model.

The second consequence is that the electron density is quite robustly determined for a lens at any valid distance. For our model, the FWHM of the density profile is about $3w$. If we take this as characteristic of the longitudinal dimension, the peak electron density $n_e \approx 500 \text{ cm}^{-3} (V_0/75 \text{ km s}^{-1})$ depends only on the velocity scale. This electron density is somewhat lower than the values estimated for shorter ESEs, in keeping with the larger inferred size.

Finally, we note that the 1-d plasma lens model predicts

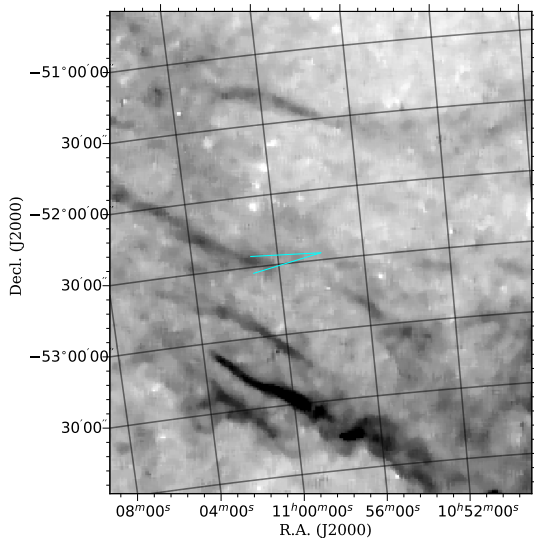


Figure 8. An H α image from SHASSA (Gaustad et al. 2001) showing the pulsar location and the cone containing its velocity vector from the measurement of Mignani et al. (2010).

chromaticity as the refraction angle $\propto \lambda^2$. We show the difference in flux densities for the two halves of our observing band as the non-solid lines in Figure 7. Although the predicted differences are relatively modest over our bandwidth, they are detectable, suggesting a more complicated lens is necessary to fully account for the data.

5 DISCUSSION

Romani et al. (1987) proposed two mechanisms to explain the observations of Fiedler et al. (1987): sheets of ionized gas in old supernova remnants whose pressures could confine sheets with $n_e \sim 50 \text{ cm}^{-3}$, sufficient to provide the observed enhancement if their aspect ratios are ~ 100 ; and very high pressure ($n_e \sim 10^4 \text{ cm}^{-3}$) magnetically-confined plasma spun off by stars. Both ideas have re-appeared recently in more generalized form. The likely ubiquity of current sheets in the ISM (Braithwaite 2015) has been invoked both to explain ESEs (Pen & King 2012) and more generally pulsar scintillation (Pen & Levin 2014). The newly-discovered strong correlation between the velocity of some intra-day variables (IDVs) and hot stars likewise lends support for a stellar origin of scattering structure (Walker et al. 2017). A unifying feature of all of these origins is substantial elongation either along or perpendicular to the line of sight, and the ESEs reported here provide further evidence for such asymmetry.

As we have described above, the ESEs towards PSR J1057–5226 and J1740–3015 have long durations and transverse sizes of $23 (V_{\text{eff}}/40 \text{ km s}^{-1}) \text{ au}$ and $80 (V_{\text{eff}}/75 \text{ km s}^{-1}) \text{ au}$, respectively. For PSR J1057–5226, the good agreement between our fiducial model and the curvature of the secondary spectrum parabola suggests the transverse size truly is at least 20 au. For J1740–3015, our fiducial model is consistent with a simple plasma lens model,

indicating a size $>20 \text{ au}$, but a wider range of values is equally good. Nonetheless, it is probably larger than 5 au, as a closer (smaller) lens would likely show pronounced annual effects from the earth’s orbit. These large sizes—and the lack of shorter/smaller ESEs in our sample—suggest the ESEs are indeed the result of inhomogeneities rather than properties of a self-similar turbulent medium.

These large transverse sizes have interesting implications for the models above. If the scatterer is sheet-like, then only inclinations close to edge-on provide the strong gradients needed to provide the refraction in PSR J1740–3015 and the sharp edges for PSR J1057–5226. Such alignment occurs by chance of order 1% of the time, consistent with the detection rates reported here (2 events/7 ESE-years per 150 pulsars/1200 source-years) and those of Fiedler et al. (1994). Further fine tuning such that the elongation is along the effective velocity yields detection rates lower than observed, suggesting that the scattering structures are roughly symmetric in the plane of the sky and overall geometry is an elongated cylinder. If the scatterer is a corrugated plasma sheet, then the corrugations are much larger than the sheet width.

There are several candidates for such extended structures along the line of sight to PSR J1057–5226. It is near the boundary of the classical Loop 1 bubble, and more convincingly along the intersection of two shells proposed by Wolleben (2007) to explain the north pulsar spur, with distances comparable to our estimate for the screen. We also note that Yao et al. (2017) place the Loop 1 shell at 195 pc, precisely at our fiducial screen distance. Inspection of an H α image (Figure 8) reveals filamentary structure on large scales, lending credence to the idea that the region may harbor such post-shock electron density enhancement as those proposed by Romani (1988) and Clegg et al. (1988). On the other hand, we note that the ESE cannot be associated with an underdensity (e.g. Pen & King 2012) since the scintillation strength increases.

Intriguingly, several type A Hipparcos stars (Perryman et al. 1997) lie both in the foreground of our 400 pc distance and within $\sim 1 \text{ pc}$ of the sight line. HIP53771 ($px=16.4(4) \text{ mas}$, $1/px=60 \text{ pc}$, $\rho=0.7 \text{ pc}$, A3III/IV, with ρ the distance from the sight line) is the strongest candidate for providing a scattering radial plasma structure (Walker et al. 2017). Two other A stars, HIP53395 ($px=8.5(3) \text{ mas}$, $1/px=120 \text{ pc}$, $\rho=0.9 \text{ pc}$, A9V) and HIP53836 ($px=7.3(4)$, $1/px=140 \text{ pc}$, $\rho=1.2 \text{ pc}$, A0V) are also candidates. In all cases, the surrounding ionized volumes are substantially smaller than their Hill spheres, so it is unclear if they are close enough. Future precise astrometry from GAIA, as well as a monitoring campaign to search for annual signatures in diffraction properties, can further test the hot star hypothesis.

Unfortunately, due to the larger and more uncertain distance to PSR J1740–3015, less can be said about specific scatterers. There are not many hot stars near earth and near the sight line, with only two Hipparcos candidates. HIP86744 ($px=8.1(3) \text{ mas}$, $1/px=120 \text{ pc}$, $\rho=1.3 \text{ pc}$, A2V) and HD316162 ($px=0.8(3)$, $1/px=1200 \text{ pc}$, 2.8 pc , A0) could plausibly provide structure along the sight line. A third Hipparcos source, HIP 86512 (A0 RR Lyr variable), has a revised GAIA distance of $\sim 1 \text{ kpc}$ (Gaia Collaboration et al. 2016) which places it too far from the sight line. Gen-

erally, we look forward to discovering more candidates with further GAIA data releases.

Although these ESEs clearly illuminate some properties of the ISM, much more could be learned, and potentially some models discarded, with additional observational data. In particular, both candidates would benefit from wideband monitoring. E.g., the ultra-wideband receiver currently being commissioned at Parkes (0.7–4.0 GHz) would expand the band to half the current observing frequency and thus will substantially increase the number of scintles observable in an observation of PSR J1057–5226. This may better characterize the refractive properties of future ESEs as well as yield better constraints on the parabolic arcs in the secondary spectrum. Conversely, the decorrelation bandwidth for PSR J1740–3015 will be resolvable above 3 GHz with even modest channelization, allowing for searches of annual modulation in diffraction which might allow association with a nearby star. In both cases, modelling the frequency evolution of the diffractive properties will allow better understanding of the turbulence spectrum dominating the scattering.

Likewise, a VLBI parallalax would greatly expand our understanding of these sources. Knowing the pulsar distance and proper motion would break the degeneracy in the lens model for J1740–3015, allowing determination of the screen location. Determining the distance of J1057–5226 would determine whether local bubble boundaries are the most likely scatterers and would give a direct measurement of the screen velocity from the parabolic arcs. Since both pulsars are bright, the measurement is possible with existing observatories.

Finally, we close with a note about the dramatic flux variations observed towards PSR J1057–5226 in its “quiescent” state, outside of the ESE. We have observed flux densities in excess (deficit) of the mean by factors of 20. Although the pulsar is not far off the Galactic plane (6.7°), the scattering is likely dominated by local material and thus many extragalactic sight lines could experience such “super” refractive scintillation if the sources are sufficiently compact. Monitoring campaigns of nearby pulsars over a range of frequencies and many refractive time-scales will reveal just how often such modulation can happen. Such substantial magnifications may play a rôle in the detectability of fast radio bursts (Macquart & Johnston 2015) and better determine the relation between FRBs and the local ISM, if indeed any exists (Fiedler et al. 1994).

ACKNOWLEDGEMENTS

We thank Phil Edwards for his deft telescope scheduling. The Parkes radio telescope is part of the Australia Telescope, which is funded by the Commonwealth Government for operation as a National Facility managed by CSIRO. This research has made use of NASA’s Astrophysics Data System, for which we are grateful. Work at NRL is supported by NASA.

REFERENCES

Abdo A. A., et al., 2013, *ApJS*, 208, 17

- Antonopoulou D., Weltevrede P., Espinoza C. M., Watts A. L., Johnston S., Shannon R. M., Kerr M., 2015, *MNRAS*, 447, 3924
- Bannister K. W., Stevens J., Tuntsov A. V., Walker M. A., Johnston S., Reynolds C., Bignall H., 2016, *Science*, 351, 354
- Braithwaite J., 2015, *MNRAS*, 450, 3201
- Brook P. R., Karastergiou A., Johnston S., Kerr M., Shannon R. M., Roberts S. J., 2016, *MNRAS*, 456, 1374
- Clegg A. W., Chernoff D. F., Cordes J. M., 1988, in Cordes J. M., Rickett B. J., Backer D. C., eds, American Institute of Physics Conference Series Vol. 174, Radio Wave Scattering in the Interstellar Medium. pp 174–178, doi:10.1063/1.37587
- Clegg A. W., Fey A. L., Lazio T. J. W., 1998, *ApJ*, 496, 253
- Clifton T. R., Lyne A. G., 1986, *Nature*, 320, 43
- Coles W. A., Rickett B. J., Codona J. L., Frehlich R. G., 1987, *ApJ*, 315, 666
- Coles W. A., Rickett B. J., Gao J. J., Hobbs G., Verbiest J. P. W., 2010, *ApJ*, 717, 1206
- Coles W., Hobbs G., Champion D. J., Manchester R. N., Verbiest J. P. W., 2011, *MNRAS*, 418, 561
- Coles W. A., et al., 2015, *ApJ*, 808, 113
- Cordes J. M., Lazio T. J. W., 2002, ArXiv Astrophysics e-prints
- Cordes J. M., Rickett B. J., Stinebring D. R., Coles W. A., 2006, *ApJ*, 637, 346
- Craig H. A., 2015, *ApJ*, 801, 24
- Fiedler R. L., Dennison B., Johnston K. J., Hewish A., 1987, *Nature*, 326, 675
- Fiedler R., Dennison B., Johnston K. J., Waltman E. B., Simon R. S., 1994, *ApJ*, 430, 581
- Gaia Collaboration et al., 2016, *A&A*, 595, A1
- Gaustad J. E., McCullough P. R., Rosing W., Van Buren D., 2001, *PASP*, 113, 1326
- Hobbs G., Lorimer D. R., Lyne A. G., Kramer M., 2005, *MNRAS*, 360, 974
- Hotan A. W., van Straten W., Manchester R. N., 2004, *Publ. Astron. Soc. Australia*, 21, 302
- Johnston S., Nicastro L., Koribalski B., 1998, *MNRAS*, 297, 108
- Johnston S., Koribalski B., Weisberg J. M., Wilson W., 2001, *MNRAS*, 322, 715
- Karastergiou A., Roberts S. J., Johnston S., Lee H., Weltevrede P., Kramer M., 2011, *MNRAS*, 415, 251
- Kaspi V. M., Stinebring D. R., 1992, *ApJ*, 392, 530
- Keith M. J., et al., 2013, *MNRAS*, 429, 2161
- Kerr M., Hobbs G., Johnston S., Shannon R. M., 2016, *MNRAS*, 455, 1845
- Lentati L., Alexander P., Hobson M. P., Feroz F., van Haasteren R., Lee K. J., Shannon R. M., 2014, *MNRAS*, 437, 3004
- Macquart J.-P., Johnston S., 2015, *MNRAS*, 451, 3278
- Maitia V., Lestrade J.-F., Cognard I., 2003, *ApJ*, 582, 972
- Mignani R. P., Pavlov G. G., Kargaltsev O., 2010, *ApJ*, 720, 1635
- Pen U.-L., King L., 2012, *MNRAS*, 421, L132
- Pen U.-L., Levin Y., 2014, *MNRAS*, 442, 3338
- Perryman M. A. C., et al., 1997, *A&A*, 323, L49
- Petroff E., Keith M. J., Johnston S., van Straten W., Shannon R. M., 2013, *MNRAS*, 435, 1610
- Rickett B. J., 1990, *ARA&A*, 28, 561
- Romani R. W., 1988, in Cordes J. M., Rickett B. J., Backer D. C., eds, American Institute of Physics Conference Series Vol. 174, Radio Wave Scattering in the Interstellar Medium. pp 156–162, doi:10.1063/1.37611
- Romani R. W., Blandford R. D., Cordes J. M., 1987, *Nature*, 328, 324
- Rookyard S. C., Weltevrede P., Johnston S., Kerr M., 2017, *MNRAS*, 464, 2018
- Shannon R. M., et al., 2014, *MNRAS*, 443, 1463
- Stinebring D. R., McLaughlin M. A., Cordes J. M., Becker K. M., Goodman J. E. E., Kramer M. A., Sheckard J. L., Smith C. T., 2001, *ApJ*, 549, L97

- Taylor J. H., Cordes J. M., 1993, [ApJ](#), 411, 674
- Tutsov A. V., Walker M. A., Koopmans L. V. E., Bannister K. W., Stevens J., Johnston S., Reynolds C., Bignall H. E., 2016, [ApJ](#), 817, 176
- Vaughan A. E., Large M. I., 1972, [MNRAS](#), 156, 27P
- Verbiest J. P. W., Weisberg J. M., Chael A. A., Lee K. J., Lorimer D. R., 2012, [ApJ](#), 755, 39
- Walker M., Wardle M., 1998, [ApJ](#), 498, L125
- Walker M. A., Melrose D. B., Stinebring D. R., Zhang C. M., 2004, [MNRAS](#), 354, 43
- Walker M. A., Tutsov A. V., Bignall H., Reynolds C., Bannister K. W., Johnston S., Stevens J., Ravi V., 2017, [ApJ](#), 843, 15
- Weltevrede P., et al., 2010, [Publ. Astron. Soc. Australia](#), 27, 64
- Weltevrede P., Wright G., Johnston S., 2012, [MNRAS](#), 424, 843
- Wolleben M., 2007, [ApJ](#), 664, 349
- Yao J. M., Manchester R. N., Wang N., 2017, [ApJ](#), 835, 29